Journal of Materials Chemistry A

ROYAL SOCIETY OF CHEMISTRY

PAPER

View Article Online
View Journal | View Issue

Cite this: J. Mater. Chem. A, 2023, 11, 7006

Hybrid polymer–liquid lithium ion electrolytes: effect of porosity on the ionic and molecular mobility†

Martina Cattaruzza, [a] Yuan Fang, [b] István Furó, [b] Göran Lindbergh, [c] Fang Liu [d] and Mats Johansson *[a]

Alternative electrolyte systems such as hybrid electrolytes are much sought after to overcome safety issues related to liquid electrolytes in lithium ion batteries (LIBs). Hybrid solid–liquid electrolytes (HEs) like the heterogeneous structural battery electrolyte (SBE) consist of two discrete co-existing phases prepared by polymerization-induced phase separation: one solid polymer phase providing mechanical integrity and the other one a percolating liquid ion-conducting phase. The present work investigates the ion and the solvent mobility in a series of HEs using morphological, electrochemical impedance and NMR spectroscopic methods. All the dried HEs exhibit a porous structure with a broad pore size distribution stretching down to <10 nm diameter. Penetration of the individual components of the solution, that is the ions and the solvent, in the solid polymer phase is demonstrated. Yet, it is the pores that are the main ion conduction channels in the liquid-saturated HEs and, in general, translational mobility is strongly dependent on the volume fraction and size of the pores and, thereby, on the initial liquid electrolyte content. We also observe that the translational mobility of solvent and the ions vary differently with the pore volume fraction. This finding is explained by the presence of small mesopores where the mobility strongly depends on the specific interactions of the molecular constituent with the pore wall. These interactions are inferred to be stronger for the EC/PC solvent than for the ions. This study shows how the morphology and the chemical composition of HEs affect the ionic and molecular transport in the system.

Received 13th January 2023
Accepted 27th February 2023

DOI: 10.1039/d3ta00250k

rsc.li/materials-a

Introduction

Lithium ion batteries (LIBs), first explored and developed by Nobel laureates of 2019 Stanley Whittingham, John B. Goodenough and Akira Yoshino,[1] have revolutionized our society toward being electrified.[2,3] The main LIB components are a negative (anode) and a positive (cathode) electrode, a separator and an electrolyte, where the latter is the main conduit for lithium ions during battery operation. The most commonly used systems employ liquid electrolytes which conventionally consist of a lithium salt dissolved in an organic solvent where the lithium ions are transported from the anode/cathode towards the cathode/anode during discharge/charge of the battery. Despite their attractive properties (such as high energy density, light weight, high ionic conductivity,[4,5] thermal stability at ambient/sub ambient temperatures, and relatively large electrochemical stability window),[6] LIBs are subject to some limitations, such as the high flammability and volatility of the organic liquid solvents used,[7] which inspired the research on alternative system components.

There are several alternative electrolytes. Polymers that can dissolve Li salts may form solid-state polymer electrolytes (SPEs).[8] Ever since Armand proposed the application of SPEs to lithium batteries,[9] a significant amount of research has been performed on this topic. Snyder *et al.* were the first to study the use of vinyl ester derivatives of poly(ethylene glycol) (PEG) for SPEs in multifunctional structural and energy storage applications.[10,11] Although SPEs have been demonstrated to be more robust compared to conventional systems, their application in commercial LIBs is limited due to their low ionic conductivity (mostly ranging between 10^{-8} and 10^{-5} S cm^{-1} at ambient temperature compared to >10^{-3} S cm^{-1} for liquid electrolytes). Ion conduction can be improved using gel polymer electrolytes (GPEs), where plasticizers/organic liquid electrolytes swell the polymer matrix and lower its glass transition temperature thereby achieving conductivity in the order of 10^{-3} S cm^{-1}.[6,12,13]

[a]Division of Coating Technology, Department of Fibre and Polymer Technology, KTH Royal Institute of Technology, SE-100 44 Stockholm, Sweden. E-mail: matskg@kth.se
[b]Division of Applied Physical Chemistry, Department of Chemistry, KTH Royal Institute of Technology, SE-100 44 Stockholm, Sweden
[c]Division of Applied Electrochemistry, Department of Chemical Engineering, KTH Royal Institute of Technology, SE-100 44 Stockholm, Sweden
[d]Division of Materials and Manufacture, Department of Industrial and Materials Science, Chalmers University of Technology, SE-412 96 Gothenburg, Sweden

† Electronic supplementary information (ESI) available. See DOI: https://doi.org/10.1039/d3ta00250k

An emerging field is hybrid electrolytes (HEs) which are defined as electrolytes composed of at least two well-defined phases. One of the phases (or even both) conducts the ions and the other phase lends mechanical stability.[14] There are several advantages to electrolytes with good mechanical properties. They make the separator unnecessary, can counteract lithium plating and short circuits and, in the case of structural batteries, are a prerequisite for their load-carrying properties. This concept leads to the use of polymer electrolyte membranes (PEMs) as an alternative to traditional liquid electrolytes in energy storage applications. In particular, Lodge *et al.* synthesized nanostructured PEMs *via* polymerization-induced phase separation (PIPS)[15,16] obtaining a satisfactory combination of mechanical and electrochemical properties.

A promising example of HEs is solid–liquid electrolytes such as the structural battery electrolyte (SBE) where two discrete phases are formed *via* PIPS.[17] The phase separation is governed by the difference in solubility parameters between the monomers and the formed polymers. At the end, a liquid ion-conducting phase percolates a thermoset structural phase where the latter provides mechanical integrity. The multifunctional properties of the SBEs showed great potential in energy-harvesting structural composite materials[18] and for structural battery applications.[19,20] Shirshova *et al.* investigated a series of SBE formulations, and demonstrated that the morphology of the porous network of structural electrolytes depends on the reaction kinetics and mechanism as well as the miscibility of the reagents, and the composition of the reaction mixture.[21,22] This is akin to other porous structures, such as controlled-pore glasses, prepared *via* phase separation.[23,24] A clear link between morphology, mechanical properties and ionic conductivity performances was proven, showing that these properties can be controlled by varying the proportion of reagents present in the resin formulation. Nevertheless, it is not fully understood how the porous structure, morphology and chemical composition affect the ion and molecular transport in HE systems.

Diffusion NMR (nuclear magnetic resonance) has been frequently used to study liquid dynamics in porous materials.[25,26] In particular, ^{7}Li (and ^{19}F) diffusion NMR has emerged as one of the most accurate techniques to obtain information about the mobility of charge carriers and lithium salt–polymer interactions in polymer electrolytes.[27–31] One specific advantage of the method is its capability to detect separately the motion of individual molecular/ionic components.

In this work, HEs with different percentages of liquid content were synthesized *via* PIPS. The mechanism of ion conduction was studied by a combination of morphological and diffusion NMR studies. The present study gives significant insight into the distribution of electrolytes inside the two-phase HEs and the factors contributing to their mobility.

Experimental

Materials

Ethylene carbonate (EC), propylene carbonate (PC), and lithium bis(trifluoromethanesulfonyl)imide (LiTFSI) (99.95% trace metal basis) were purchased from Sigma-Aldrich. The monomer bisphenol A ethoxylate dimethacrylate (BPAMA) (M_n: 540 g mol^{-1}) was donated by Sartomer (Arkema Group). Chemical structures are shown in Fig. S1 of the ESI.† Lithium standard 1000 mg L^{-1} in nitric acid (TraceCERT®) and 2,2′-azobis(2-methylpropionitrile) (AIBN) were purchased from Sigma-Aldrich. All materials were used as received.

Hybrid solid–liquid battery electrolyte and BPAMA polymer film preparation

A series of HEs as well as reference samples of the bulk polymer (pBPAMA) alone were prepared according to the following procedure. All samples were prepared inside a glovebox under a dry argon atmosphere (<1 ppm H_2O, <1 ppm O_2). The liquid electrolyte was prepared by mixing PC with EC at 50 : 50 wt%, the latter pre-heated to 60 °C. The lithium salt LiTFSI was then added into the solvent mixture at 1 M concentration.

For the HE film preparation, the electrolyte prepared was mixed with the monomer BPAMA and with the thermal initiator AIBN. The AIBN content was 1 wt% relative to the monomer content. The liquid electrolyte content varied between 40 wt%, 45 wt% and 50 wt% of the total weight.

For pBPAMA film preparation the monomer was mixed with 1 wt% AIBN and with a small amount (around 10 wt%) of the solvent (EC : PC 50 : 50 wt%) for the initiator dissolution. The chemicals were stirred until a homogeneous mixture was obtained.

The HE and pBPAMA resins were then poured into an aluminium mold (30 × 6 × 0.5 mm^3) and covered with a glass slab. The specimens were subsequently clamped on both edges and vacuum-sealed into a pouch bag inside the glovebox. Finally, the bagged samples were transferred out of the glovebox and directly thermally cured at 90 °C for 45 min in a preheated oven. Henceforth, the prepared HE samples are denoted, respectively, as HE 40 wt%, HE 45 wt%, and HE 50 wt%.

Fourier transform infrared spectroscopy

A PerkinElmer Spectrum 100 instrument equipped with a deuterated triglycine sulfate detector was used to determine the double bond conversion by Fourier-transform infrared spectroscopy (FTIR). The instrument was equipped with a single reflection attenuated total reflection (ATR) accessory unit, with a diamond ATR crystal (Golden Gate) from Graseby Specac Ltd. The data were analyzed using Spectrum software v. 10.5.1 from PerkinElmer. Two samples of each formulation were analyzed both before and after curing with 16 scans with a resolution of 4 cm^{-1} performed for each spectrum. The conversion of the acrylate groups was determined by comparing the area under the vinyl peak at 1637 cm^{-1} of uncured resin and cured films. The carbonyl peak of the ester group at 1715 cm^{-1} was used as the internal reference for all spectra (see details in the ESI†).

Gravimetric analysis of leached HEs

The formation of the percolating polymer phase was evaluated for the different formulations of HEs. All samples were soaked in abundant water (240 mL which corresponded to a water-to-sample mass ratio of 2.6) for one week in order to remove the

liquid electrolyte (EC, PC and LiTFSI). The samples were then dried in a vacuum oven at 60 °C for one week. Mass loss quantification was performed by weighing the samples before immersion into water and after drying using a scale with a resolution of 0.1 mg. Two samples of each formulation were tested.

Gravimetric and NMR analysis of swelling and leaching of bulk polymer samples

The swelling and leaching of the pure polymer were evaluated both gravimetrically and with NMR analysis. All sample preparation was performed inside a dry argon glovebox.

Films of pBPAMA were soaked into different electrolyte formulations in order to quantify if and to what extent the electrolyte and/or the solvent penetrates and swells the thermoset polymer.

The tests were performed with:

- 50 : 50 wt% EC : PC without salt.
- 1 M LiTFSI in 50 : 50 wt% EC : PC (same salt concentration as used for the hybrid electrolytes).
- 2 M LiTFSI in 50 : 50 wt% EC : PC.

The films were first cut to size (approximately 10 × 3 × 0.5 mm^3). The cut specimens were soaked in the aforementioned liquids and their respective masses were recorded before soaking and then every second day until reaching saturation. Prior to weighing, the surface of the soaked samples was carefully dried with tissue to remove all the liquid cover.

The amount of solvent and salt absorbed by pBPAMA was further quantified with NMR. pBPAMA samples were transferred into NMR tubes, to which 0.6 mL acetonitrile-d3 was added before sealing airtight. The solvent molecules and the ions taken up by bulk pBPAMA exhibit slower molecular dynamics and, therefore, very broad NMR peaks that remain undetectable (proven by separate experiments on the films before acetonitrile was added, see Fig. S2†) under the conditions set. Hence, any high-resolution liquid NMR signal detected from solvent and salt arose from those species released from pBPAMA into the liquid surrounding the films. The amount of EC/PC released was followed by ^{1}H NMR *via* the peak integral at 4.52 ppm for EC and at 4.85/4.02 ppm for PC (see peak assignments in Fig. S3†). The amount of LiTFSI released was followed by ^{19}F or ^{7}Li NMR (with the Li : TFSI molar ratio set strictly to 1 : 1 by electroneutrality). Two samples of each formulation were measured.

The NMR measurements were conducted with a Bruker Avance III spectrometer at 11.7 T, equipped with a Bruker DIFF 30 probe. Single-pulse experiments with a 90° pulse and with the delay time set to over five times the respective longitudinal relaxation time were carried out. 16 scans were collected for each measurement. Samples were gently shaken between measurements. All the measurements were conducted at 298 K. Quantitative data were obtained by relating the solvent (^{1}H) and salt (^{7}Li and ^{19}F) spectral integrals to those from, respectively, ^{1}H (10 mg EC and 10 mg PC dissolved in 0.6 mL acetonitrile-d3), ^{7}Li (TraceCERT®, 1000 mg L^{-1} Li ions in dilute nitric acid) and ^{19}F (1 M LiTFSI in EC : PC 1 : 1) external standard samples. The uncertainty was estimated from the signal-to-noise ratio of the respective peaks in the sample as shown in ref. 32 (see Fig. 4).

NMR quantification of liquid electrolyte removal from HE

A sample prepared with 45 wt% liquid electrolyte content was first cut to size (approximately 10 × 3 × 0.5 mm^3) to fit at the bottom of the NMR tubes. 0.6 mL of DMSO-d6 was added prior to sealing the tube airtight. In contrast to pBPAMA, the solvent molecules and the ions within the pores of the HE are highly mobile and provide narrow NMR peaks. To detect release, the NMR tubes were placed in the probes so that the HE pieces were far below the active volume of the radiofrequency coil. Hence, any high-resolution liquid NMR signal detected arose from molecules and ions released into the added DMSO-d6 whose liquid column extended far above the HE pieces and into the active volume. Subsequently, the amounts of solvent and salt released from the film were followed by ^{1}H and ^{7}Li NMR or ^{19}F with the procedure specified in the section above. One sample was tested for this analysis.

Scanning electron microscopy (SEM) and broad ion beam milling combined with scanning electron microscopy (BIB-SEM)

In order to investigate the morphology and microstructure of the HEs and compare them to pBPAMA, SEM was performed on the samples. Before analysis, the samples were leached into water for 24 h in order to extract the liquid electrolyte. The samples were then dried in a vacuum oven overnight at 60 °C.

In order to compare their morphology and microstructure, the HE and pBPAMA samples were submerged in liquid nitrogen and cryo-fractured. The cross-sections of cured HE films were analyzed using a Hitachi SEM S-4800 microscope equipped with a cold field-emission electron source. The fractured cross-sections were mounted on an SEM sample holder with conductive carbon tape and they were subsequently coated with Pt/Pd using a Cressington 208HR sputter coater for 20 s (corresponding to ≈3 nm of the conductive coating layer, measured with a quartz crystal microbalance) at a current of 80 mA. The images were captured with an accelerating voltage of 1 kV at a working distance of 8–9 mm.

In the International Union of Pure and Applied Chemistry (IUPAC) classification of pore size, the micropore width does not exceed 2 nm (20 Å), the mesopore width is in the range 2–50 nm and the macropore width is above 50 nm.[33] Such small pore sizes are difficult to visualize. In order to better reveal the porous structure without the interference from surface morphology of the fractured cross sections, a Leica EM TIC 3X triple ion-beam cutter was used to produce a large (up to a few mm^2), fine ion-polished HE surface for SEM analysis. A piece of the HE sample (~5 mm wide) was adhered to a Si wafer with similar size. The Si wafer provides a perfectly flat mask, which ensures a high-quality polish on the HE. In order to reduce the possible ion damage and thermal effect introduced by ion bombardment and at the same time balance the ion milling time, the argon ion source was set at an energy of 5–5.5 kV. The fine ion-polished surfaces were analyzed using a Zeiss Gemini

450 SEM. The SEM is equipped with a field emission electron gun. To mitigate the charging effect, an accelerating voltage of 1 kV was used at a working distance of 3–4 mm. The images with high resolution were recorded using an in-lens secondary electron detector. The equivalent average diameter values were calculated based on 270 pores from the 40% sample and 306 pores from the 50% sample. All the pores located at the edges of the SEM micrographs were excluded in the measurement in order to obtain a more accurate estimation of the pore size. Image analysis was carried out using an in-house Python program.

Electrochemical impedance spectroscopy (EIS)

Electrochemical impedance spectroscopy (EIS) was used to quantify the ionic conductivity of both the HE and the liquid electrolyte at ambient temperature. The measurement was performed inside a glovebox just after respective sample preparations so that the effect of solvent evaporation was minimized.

For the HE films, the analysis was conducted using a Gamry Series G 750 potentiostat/galvanostat/ZRA interface. The setup utilized consisted of a four-point electrode cell with gold wires as electrodes, two working electrodes (20 mm apart) and two reference electrodes (5 mm apart). The impedance was measured in the frequency range of 120 kHz to 1 Hz. The bulk resistance (R_b) was obtained from the low-frequency intercept on the real axis in the resulting Nyquist plot. The ionic conductivity σ was calculated as $\sigma = \frac{l}{R_b A}$ where l is the length between the reference electrodes (5 mm), R_b is the bulk resistance and A is the cross-sectional area of the sample. The cross-sectional area was estimated from the thickness and width of each sample measured by using a digital slide caliper. Three samples of each formulation were tested. Detailed error estimates were omitted because of the large (approx. 10%) inaccuracy of the thickness.

For the pure liquid electrolyte formulations, the ionic conductivity values were measured using a Mettler Toledo SevenCompact™ Conductivity S230 meter with an internal conductivity standard. Two samples of each formulation were tested.

Ion mobility studies with NMR

The HE specimens were cut to size (approximatively 10 × 3 × 0.5 mm^3) to fit into the NMR tubes. ^{7}Li, ^{1}H and ^{19}F NMR measurements were performed with a Bruker Avance III 500 MHz spectrometer equipped with a 5 mm DIFF probe.

Diffusion measurements were carried out using a GREAT60 gradient power supply that provides a maximum z-gradient strength of 1800 G cm^{-1} for the probe used. A stimulated echo pulse sequence was used with gradient duration δ set between 0.8 and 1.0 ms, diffusion time Δ set to 200 ms for ^{19}F (in the anion), to 1000 ms for ^{1}H (in the solvent) and to 800 ms for ^{7}Li (in the cation) measurements. The gradient strength g was stepped up from 5 to 500 or 1300 G cm^{-1} for different samples in 10 steps. The diffusional decay was fitted using the Stejskal–Tanner expression $S/S_0 = \exp\left(-\gamma^2\delta^2 g^2 D\left[\Delta - \frac{\delta}{3}\right]\right)$ to obtain the diffusion coefficient D,[34] where γ is the magnetogyric ratio and S and S_0 represent the integral intensities with and without gradient g, respectively. Typical diffusional decay for each nucleus is shown in Fig. S4.† All diffusion measurements were performed at 298 K. The error of diffusion coefficient was estimated to be 4–5% from the uncertainty derived when fitting the Stejskal–Tanner expression to the data using the Levenberg–Marquardt method. One sample of each formulation was tested.

Results

Curing performance

Fig. 1 shows the FTIR spectra of HE 50 wt% before and after curing. The shift of the carbonyl peak from 1715 cm^{-1} before curing to 1725 cm^{-1} after curing is related to the C=O bond frequency change caused by the disappearance of the neighboring C=C vinyl peak (at 1637 cm^{-1}) during the polymerization. The lower absorbance of the carbonyl after curing also means that the conversion is underestimated when using the carbonyl as an internal standard. FTIR spectra of the other formulations which show a similar behavior are shown in Fig. S5–S7 of the ESI.† It has previously been shown by Johansson *et al.*[35] that thermal curing under the aforementioned conditions is a robust method for the PIPS in HE systems.

The FTIR results (Table 1) show that a very high conversion of the double bond was achieved for all hybrid electrolytes. For the bulk pBPAMA sample the conversion achieved was lower due to vitrification. This phenomenon is the transition from the rubber state to the glass state that occurs when the molecular weight of the forming polymer exceeds what is thermodynamically stable as a rubber.[36]

The phenomenon causes a drastic slowdown of the reaction because of the reduced mobility of the reactants. In the hybrid electrolyte samples there is solvent present in the vicinity of the forming polymer chains, though at a concentration that is continually decreasing with increasing degree of

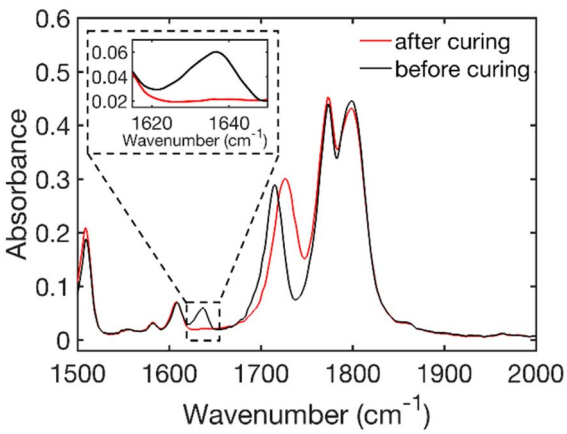

Fig. 1 FTIR spectra of the resin (before curing) and of the film (after curing) showing the disappearance of the vinyl stretch peak at 1637 cm^{-1} (see the enlarged region) for HE 50 wt%.

Table 1 The average conversion of the different formulations calculated from FTIR peak intensities

Sample	Average conversion [%]
HE 40 wt%	95 ± 1
HE 45 wt%	96 ± 1
HE 50 wt%	95 ± 2
pBPAMA	83 ± 2

polymerization and thus increasing phase separation. This feature should plausibly delay vitrification.

Characterization of HE morphology

The morphology of the different HE formulations and pBPAMA was studied by SEM. Images of cryo-fractured HE 40 wt% and of pBPAMA are compared in Fig. 2. The SEM images of the other formulations are shown in Fig. S8 of the ESI.†

As can be seen from Fig. 2, the HE is composed of porous structures. In contrast, pBPAMA exhibits a compact structure and a smooth surface. Among different HE compositions, there is no significant variation in morphology detectable in the SEM images (Fig. S8†). However, it is impossible to compare the pore structure of HEs in detail with different formulations due to the complex surface topography, which smears the information of the pores. Note that SEM has limitations for the analysis of porous structures which are (i) SEM provides an image of a dried sample, which is not the actual electrolyte condition during the battery operation, (ii) the SEM image is a 2D projection of a small portion of the specimen and (iii) it is unclear how the fractured surface is affected by the sample preparation. Hence the images should be considered as qualitative rather than quantitative regarding pore space and interconnectivity.

To overcome these difficulties, we also performed ion polishing on the cross-sectional surfaces using a BIB. Two different HE formulations were studied by BIB-SEM. The samples analyzed had an electrolyte content of 40 wt% and 50 wt% since they are the two extreme specimens studied in the present study. Images are illustrated in Fig. 3 and in Fig. S9 of the ESI.† The milled surfaces of both specimens show macropores and mesopores (ranging from 200 nm down to <10 nm) and the samples look homogeneous (as can be seen in the image with lower magnification Fig. 3a) on the micrometer scale. The equivalent average diameter of the pores is 41 nm for the 40% sample and 48 nm for the 50% sample. This interconnected porous network filled with electrolyte is the ion transport pathway and lends ion conductivity to the HEs.

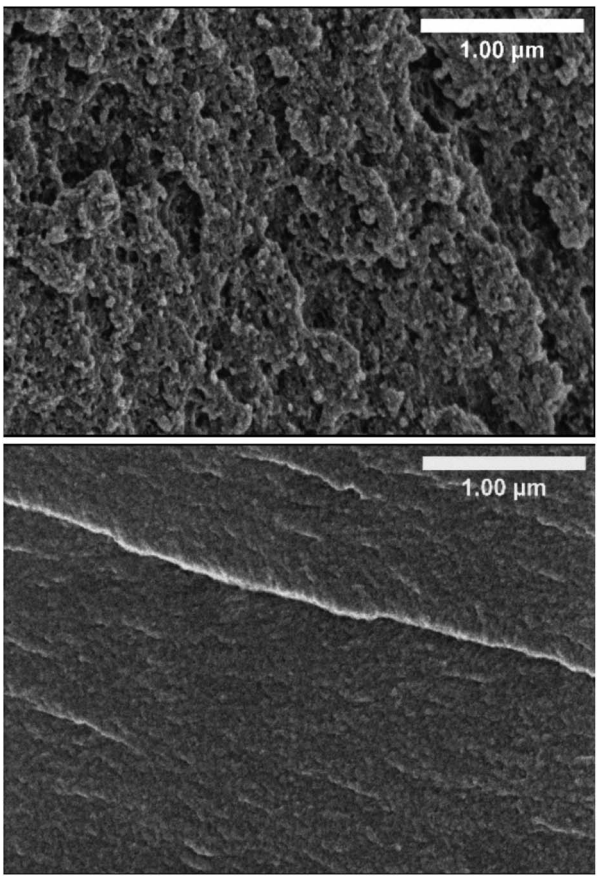

Fig. 2 Cross-sectional SEM micrographs of cryo-fractured HE 40 wt% (top) and of pBPAMA (bottom). All samples were dried beforehand.

Electrolyte in HEs

To investigate how electrolytes are distributed inside HEs and their relation to ion-conduction, we quantified the amount of LiTFSI and EC/PC in HEs and pBPAMA in detail. It has previously been proposed that the HE is a two-phase system with liquid electrolyte as one phase and a thermoset polymer phase as the other as determined by gravimetric analysis of similar systems.[17] As HEs already contain a nominal composition of 40–50 wt% electrolyte, the amount of LiTFSI and EC/PC was determined by a release test. That is, HEs of different formulations were soaked in deionized water for 7 days to remove the electrolytes. The samples were then dried and weighed. The weight difference of HEs before and after soaking is ascribed to the electrolyte content in HEs as summarized in Table 2.

Clearly, most of the electrolytes can be removed from HEs confirming the co-existence of two phases for the present system. This also confirms the nominal composition of HEs with a deviation of less than 3%. Therefore, the loss of electrolyte during the curing process is very small if any.

Conversely, the single-phase pBPAMA films prepared were soaked in LiTFSI in PC/EC of different concentrations (see Table 3) for 7 days to allow electrolyte components to be absorbed until the film weight reached saturation. The films before and after soaking were weighed using a scale and the results are summarized in Table 3.

While LiTFSI determines conductivity, it constitutes only a small weight fraction of the electrolyte. Hence, the magnitude of LiTFSI and also EC/PC release from HEs and soaked pBPAMA were quantified separately by NMR experiments (see the Materials and methods). In the tests, the HE 45 wt% and soaked

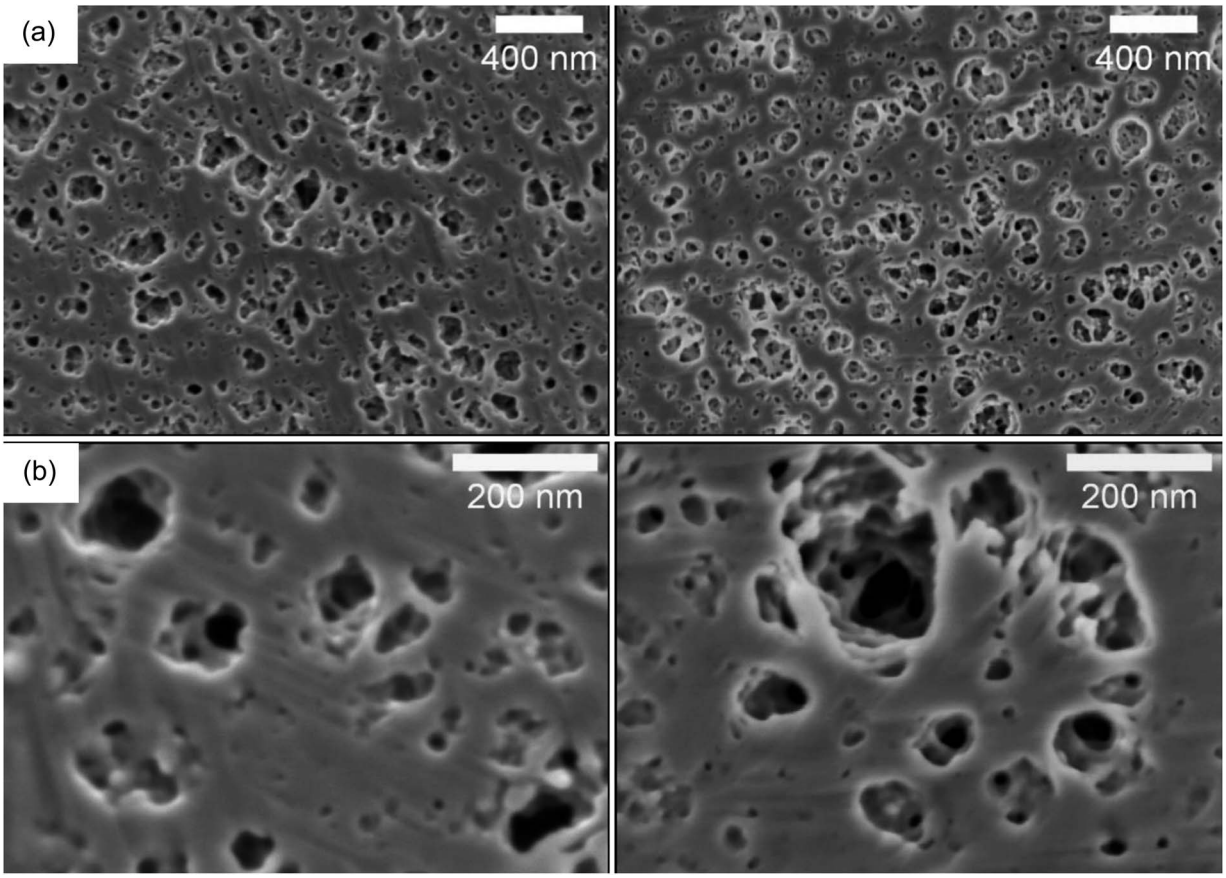

Fig. 3 BIB-SEM images of the 40 wt% (left) *vs.* 50 wt% (right) electrolyte content HEs at (a) lower magnifications (b) higher magnifications.

Table 2 Gravimetric analysis of electrolyte release from HEs

Sample	Mass loss during release [wt%]	Difference between the initial content and released electrolyte amounts [wt%]
HE 40 wt%	38.2 ± 0.4	1.8
HE 45 wt%	42.2 ± 0.2	2.8
HE 50 wt%	47.3 ± 0.1	2.7

pBPAMA were immersed in DMSO-d6 and acetonitrile-d3 respectively. The released LiTFSI amount was monitored by quantitative ^{7}Li or ^{19}F NMR (assuming $Li^{+}:TFSI^{-} = 1:1$ required by electroneutrality). The released amount of EC and PC was monitored by quantitative ^{1}H NMR of respective peaks (see Fig. S2†). The time courses of release are illustrated in Fig. 4 and the final values are summarized in Table 3.

Interestingly, we find that both the solvent EC/PC and the lithium salt LiTFSI can be absorbed into the bulk polymer phase and the uptake is around 8–10 wt% of electrolyte. This "swelling" occurs when a dry polymer is immersed in a solvent whose molecules can reversibly penetrate the polymer network and, consequently, expand it. However, the process reaches equilibrium set by the elastic forces of the cross-links (either physical or chemical) that counter-balance the volume expansion, thereby stopping further solvent absorption.[37] Such swelling is not uncommon.[38] The electrolyte content in HEs is much higher than in pBPAMA, 40–50 wt%. This is because HEs have a porous network which imbibes the bulk

Table 3 The mass of pBPAMA before and after soaking. The amount of solvent and salt released from soaked pBPAMA films

Electrolyte concentration [M]	Mass before soaking[a] [mg]	Mass after soaking[a] [mg]	PC mass[b] [mg]	EC mass[b] [mg]	LiTFSI mass[b] [mg]	Concentration of absorbed LiTFSI[c] [M]
0	40	42	2.42	1.43	—	—
1	32	34	1.11	1.16	0.21	0.32
2	32	34	1.20	1.22	0.16	0.23

[a] Determined by gravimetric measurements. [b] Determined by ^{1}H or ^{7}Li NMR. [c] Defined as the amount of absorbed LiTFSI relative to the absorbed solvent EC/PC (see details in the ESI).

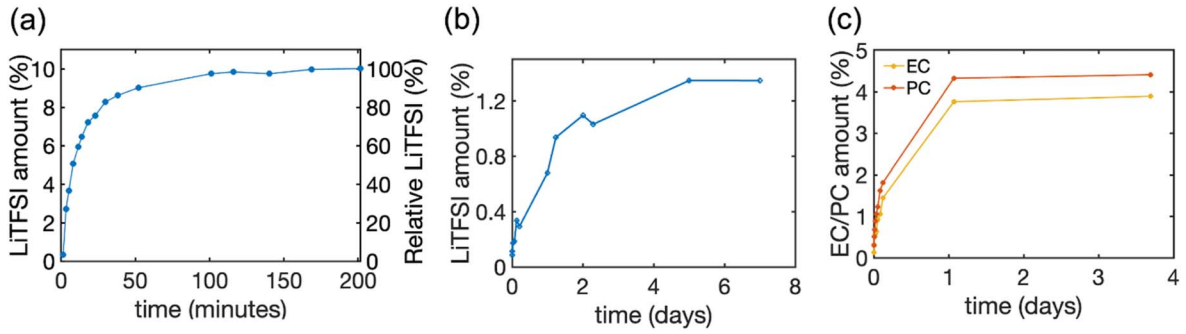

Fig. 4 The amount of LiTFSI salt and solvent released from HE and pBPAMA. (a) The amount of LiTFSI released from HE 45 wt% to DMSO-d6 determined by ^{19}F NMR. (b) The amount of LiTFSI released from pBPAMA to acetonitrile-d3 determined by ^{7}Li NMR. (c) The amount of PC/EC released from pBPAMA to acetonitrile-d3 determined by ^{1}H NMR. The LiTFSI amount on the left *y*-axis is the mass of LiTFSI relative to the total mass of the sample. The relative LiTFSI on the right *y*-axis is the mass of LiTFSI relative to the nominal LiTFSI content of the HE. The final released amount in mass units is presented in Table 3. The measurement uncertainty varies with the NMR signal-to-noise ratio[32] and thereby the uncertainty of the measurements decreases from around 15–20% for the initial points until 0.4% LiTFSI amount, to around 5% for LiTFSI amount of more than 0.9%.

liquid electrolyte. Due to the same reason, electrolyte release from HEs and soaked pBPAMA is also very different, see Fig. 4. In HE 45%, most of the LiTFSI was released in the first hour and more than 99 wt% of the LiTFSI was extracted within three hours. This indicates a continuous pore network within which the electrolyte transport is fast. The soaked pBPAMA film on the other hand shows much slower release because the dynamics of the solvent molecule transport (not as bulk liquid but, presumably, individual molecules or very small clusters) within the polymer network is much slower. This is corroborated by the loss of the NMR signal of the molecules swelling the pBPAMA (see above).

The data above suggest that a small fraction of the electrolyte exists not only in the porous structures but also in the polymer phase. Notably, the individual compositions in Table 3 show that PC and EC were absorbed by pBPAMA with almost a 1 : 1 weight ratio and both were absorbed preferably compared to LiTFSI. This is evidenced by the fact that the equivalent (relative to the absorbed solvent) concentration of absorbed LiTFSI is around 0.2–0.3 M, which is far below the salt concentration (1 M/2 M) in the original electrolyte.

The ionic conductivity and ion conduction mechanisms in the HE

The ionic conductivity values of the different HE formulations are summarized in Table 4. It can be seen that liquid electrolyte has a conductivity one to two orders of magnitude higher than that of the HE samples; by decreasing the electrolyte content from 50 wt% to 40 wt%, the conductivity decreased sevenfold. The decrease of conductivity is generally consistent with expectations based on the known structure since the liquid phase of the HE is ion conducting while the polymer phase does not contribute significantly to ion conduction. It is however surprising that by increasing from 40 wt% to 50 wt% the increase in conductivity is far more than the proportion of the electrolyte-filled pore volume.

Table 4 Ionic conductivity results from the EIS measurement

Sample	Conductivity [S cm^{-1}]
1 M LiTFSI	4.3×10^{-3}
HE 40 wt%	3.7×10^{-5}
HE 45 wt%	1.4×10^{-4}
HE 50 wt%	2.9×10^{-4}

In order to elucidate the molecular mechanism responsible for this sharp increase, we analyzed the self-diffusion of the cation (Li^+), anion ($TFSI^-$) and the solvent (PC and EC) inside the HE by ^{7}Li, ^{19}F and ^{1}H NMR diffusion experiments, respectively. We note here that the solvent data were recorded for the composite peak at 4.52 ppm, see Fig. S2,† that is dominated by the signal from the EC molecules. Yet, the diffusion coefficients of the PC and EC molecules in the solvent differ by just a few percent, see the ESI.† The obtained self-diffusion coefficients are summarized in Fig. 5a and Table S1† and show that the Li^+, $TFSI^-$ and the carbonate molecules all diffuse faster in the HE with higher electrolyte content and they correlate well with conductivity values. A correlation between conductivity and increasing amount of electrolyte was also observed in porous gel electrolytes.[39]

The transference number was also calculated as:

$$t^+ = \frac{D^+}{D^+ + D^-}$$

where D^+ and D^- are the diffusion coefficients of Li^+ and $TFSI^-$, respectively. The calculated values are summarized in Table 5. The transference number increases with increasing electrolyte content. However for HE 50 wt%, its transference number is already close to the transference number of the only-liquid 1 M electrolyte.

Yet, the striking feature of the diffusion data, as shown in Fig. 5b is that the reduction in the solvent diffusion relative to the respective value in bulk is far larger than that of Li^+ and $TFSI^-$ diffusion. This observation in combination with the very

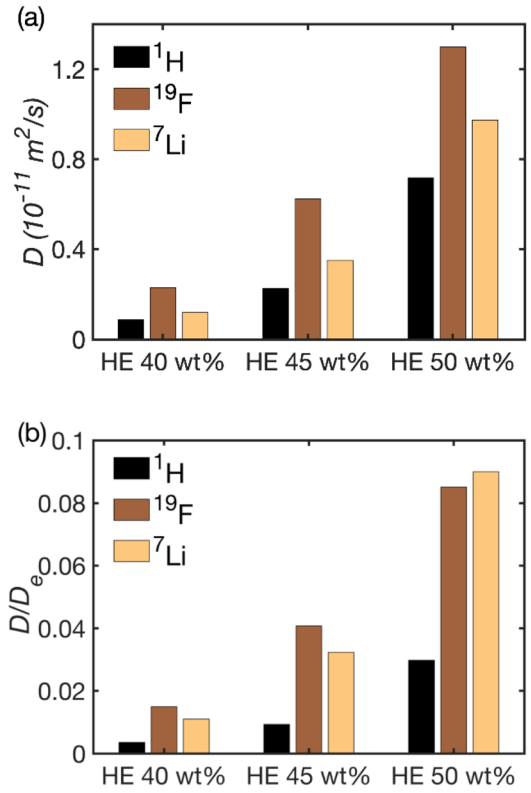

Fig. 5 (a) The self-diffusion coefficients of ^{1}H (solvent), ^{19}F (anion) and ^{7}Li (cation) determined in HEs 40 wt%, 45 wt% and 50 wt%. (b) The ratio of ionic/molecular self-diffusion coefficients in HEs *vs.* their respective bulk value in 1 M LiTFSI in EC/PC.

Table 5 Transference number in bulk and in HEs

Sample	Transference number t^+
1 M LiTFSI	0.41
HE 40 wt%	0.34
HE 45 wt%	0.36
HE 50 wt%	0.43

strong dependence of conductivity and diffusion on the fraction of pores in the system poses a question on which structural features could be their cause. There are several molecular mechanisms that can contribute to the observed behavior.

A possible mechanism is the molecular exchange of both ions and solvent molecules between the electrolyte in the pores and in the polymer phase. If (i) that exchange is fast or comparable to the explored diffusion time (Δ = 200–1000 ms, depending on the nucleus, see above) and (ii) the diffusion of those species is slow in the polymer phase, the population average of the diffusion coefficients would be below the value observed in the bulk electrolyte. Yet, that average coefficient would vary in proportion to the surface-to-volume ratio of the pores (that is, over the initial electrolyte content) and that variation must be far weaker than the experimental observation shown in Fig. 5b. Hence, this mechanism is discarded.

Another possible mechanism also involves the partition of the electrolyte components into the polymer matrix and invokes pore closures (pore blocking) that is, moreover, becoming more frequent in the structures with large amounts of smaller pores.[25] Such pore closures are more likely to be formed with a lower initial electrolyte content. To have a significant influence over the observed behavior, pore closures must be significant (explored several times) features within the region set by the average diffusional displacement, set in turn by the diffusion time Δ and the diffusion coefficient D as $(6D\Delta)^{1/2}$. This value is in the order of μm in our system (the actual value varies between 2 and 4 μm with the sample and the nucleus observed). When the different species encounter a pore closure that behaves like a barrier, the latter can only be passed if the species involved have a non-zero solubility in the barrier. In the present system, this barrier is the polymer phase. The data in Table 3 (last column) show that the solvent solubility in the polymer matrix is higher than that for LITFSI. Yet, the barrier permeability should increase with increasing solubility while we observed the opposite (Fig. 5). Hence, this mechanism is considered to be unlikely.

In the present study, the hypothesis that is considered as most likely involves no pore closures but the formation of very narrow (<10 nm) channels that appear with increasing frequency with decreasing electrolyte content. Again, to exert a significant influence, such narrow channels must be significant (explored several times) features within the region set by the average diffusional displacement. Mesopores were indeed observed in abundance in the BIB-SEM images. In such narrow channels, the specific interactions of the species with the wall has a very strong effect on the diffusion coefficient[25] as has been demonstrated also for solvents and ions.[40] To be able to reproduce the observed behavior, interactions between the channel walls and the solvent molecules that are stronger than the ones between the walls and the ions are needed. Indeed, this is consistent with the observed preferential absorption of the solvent by pBPAMA.

Discussion

Nano-channels are often introduced into polymer systems *via* various routes to enhance their conductivity and such interconnected channels are believed to create fast Li-ion conduction pathways. One way to achieve this is to add nano-sized fillers, such as inorganic particles and nanowires,[41,42] yielding composite solid-state electrolytes. Channels can also be created by etching.[43] In the present system, porous structures are formed spontaneously through a polymerization induced-phase separation process. The pore sizes vary from <10 nm to hundreds of nanometers. The presence of pores facilitates ion conduction while retaining the macroscopic mechanical integrity thereby lending multiple functionalities to lithium batteries. Though the micro- and mesopores are hard to quantify (especially so in the liquid-filled case with a swollen matrix where gas sorption methods are less suitable), the influence of such pores is also significant because the effect of specific interactions between the electrolyte and the polymer wall on

transport becomes more significant at smaller pore diameters.[25] Such specific interactions depend on the chemical identity and could be tuned if the chemical structures of either the electrolyte or the polymer wall are modified. Indeed, this phenomenon is implicated here for the chemically specific slowing-down of the diffusion of the different electrolyte components in the HEs produced.

Finally, the question appears what mechanism provides narrower (or, far narrower or both) channels in the system with low (40 wt%) electrolyte content than that in the system with high (50 wt%) electrolyte content. While a final answer cannot be provided, an interesting feature can be pointed out. First, there are well-known and extensively studied porous systems, namely controlled-pore glasses, whose porous network is produced by phase separation, specifically as a result of the spinodal decomposition of two oxide phases.[23,24] In such glasses, the pore topology is largely invariant and weakly dependent on composition.[44–46] In other words, the pore systems look the same except every feature (pores as well as the matrix) being magnified by the same factor depending on the phase separation time (ripening). In such systems, one would expect no drastic increase of the presence of narrow channels by decreasing the proportion of pore volume by merely 20% (corresponding to the decrease of the initial electrolyte volume from 50 wt% to 40 wt%). Yet, in controlled pore glasses, the phase separation stage and the solidification stage are distinct. This is not the case for the present system where the phase separation is driven by the ongoing polymerization but, at the same time, that feature also increasingly immobilizes the molecules in the matrix as polymerization proceeds. In other words, the same mechanism, polymerization, is both the driving and the blocking force of phase separation. The structural features obtained under such conditions seem to be smaller and/or more numerous channels in the meso/micropore size range at a higher initial polymer content.

Conclusions

In this paper, morphology features and conductivity were coupled with NMR analysis in order to explore the relation between structure and performance of hybrid solid–liquid lithium ion electrolytes. Both the solvent EC/PC and the lithium salt LiTFSI were proved to be absorbed into the bulk polymer phase and the uptake is around 8–10 wt% of electrolyte. Solvent molecules were demonstrated to be absorbed in the polymer phase preferentially to LiTFSI. Self-diffusion coefficients determined by NMR correlate well with the ionic conductivity measurements and demonstrate higher molecular and ionic mobility in electrolyte species with higher liquid electrolyte content. Morphological studies show the presence of very narrow pores (<10 nm) formed during the polymerization of systems. In such narrow channels, the interactions of the electrolyte species with the pore wall seems to have a very strong effect on their mobility. The combined results show that the electrochemical performance of HEs depends on the chemical interaction between the liquid and the solid phase and on the nm-scale morphology of the structure.

Conflicts of interest

There are no conflicts to declare.

Acknowledgements

The Swedish Energy Agency (grant #48488) and the Swedish Research Council VR are gratefully acknowledged for financial support.

References

1 A. Yoshino, *Bull. Chem. Soc. Jpn.*, 2022, **95**, 195–197.
2 J. Xie and Y. C. Lu, *Nat. Commun.*, 2020, **11**, 2499.
3 K. Keramidas, M. Tamba, A. Diaz-Vazquez, X. Wen, Q. Chai, R. Van Dingenen, S. Tchung-Ming, J. Krause, T. Vandyck, A. Soria-Ramirez, S. Fu and M. Weitzel, *Global Energy and Climate Outlook 2019*, Publications Office of the European Union, 2020.
4 D. Zhou, D. Shanmukaraj, A. Tkacheva, M. Armand and G. Wang, *Chem*, 2019, **5**, 2326–2352.
5 K. Xu, *Chem. Rev.*, 2004, **104**, 4303–4418.
6 A. Arya and A. L. Sharma, *Ionics*, 2017, **23**, 497–540.
7 M. Piglowska, B. Kurc, M. Galinski, P. Fuc, M. Kaminska, N. Szymlet and P. Daszkiewicz, *Materials*, 2021, **14**, 6783.
8 B. Sun, J. Mindemark, K. Edström and D. Brandell, *Solid State Ionics*, 2014, **262**, 738–742.
9 M. Armand, J. Chabagno and M. Duclot, *Presented in Part at the Second International Meeting on Solid Electrolytes*, St. Andrews, Scotland, September 20–22, 1978.
10 J. F. Snyder, R. H. Carter and E. D. Wetzel, *Chem. Mater.*, 2007, **19**, 3793–3801.
11 J. F. Snyder, E. D. Wetzel and C. M. Watson, *Polymer*, 2009, **50**, 4906–4916.
12 S. Liang, W. Yan, X. Wu, Y. Zhang, Y. Zhu, H. Wang and Y. Wu, *Solid State Ionics*, 2018, **318**, 2–18.
13 J. Y. Song, Y. Y. Wang and C. C. Wan, *J. Power Sources*, 1999, **77**, 183–197.
14 M. Keller, A. Varzi and S. Passerini, *J. Power Sources*, 2018, **392**, 206–225.
15 M. W. Schulze, L. D. McIntosh, M. A. Hillmyer and T. P. Lodge, *Nano Lett.*, 2014, **14**, 122–126.
16 L. D. McIntosh, M. W. Schulze, M. T. Irwin, M. A. Hillmyer and T. P. Lodge, *Macromolecules*, 2015, **48**, 1418–1428.
17 N. Ihrner, W. Johannisson, F. Sieland, D. Zenkert and M. Johansson, *J. Mater. Chem. A*, 2017, **5**, 25652–25659.
18 R. Harnden, D. Carlstedt, D. Zenkert and G. Lindbergh, *ACS Appl. Mater. Interfaces*, 2022, **14**, 33871–33880.
19 L. E. Asp, K. Bouton, D. Carlstedt, S. Duan, R. Harnden, W. Johannisson, M. Johansen, M. K. G. Johansson, G. Lindbergh, F. Liu, K. Peuvot, L. M. Schneider, J. Xu and D. Zenkert, *Adv. Energy Sustainability Res.*, 2021, **2**, 2000093.
20 L. E. Asp, M. Johansson, G. Lindbergh, J. Xu and D. Zenkert, *Funct. Compos. Struct.*, 2019, **1**, 042001.
21 N. Shirshova, A. Bismarck, E. S. Greenhalgh, P. Johansson, G. Kalinka, M. J. Marczewski, M. S. P. Shaffer and M. Wienrich, *J. Phys. Chem. C*, 2014, **118**, 28377–28387.

22 N. Shirshova, T. Rogaume, H. Najmi and M. Poisson, *Fire Mater.*, 2021, **46**, 192–204.
23 W. Haller, *Nature*, 1965, **206**, 693–696.
24 R. Schnabel and P. Langer, *J. Chromatogr. A*, 1991, **544**, 137–146.
25 F. Elwinger, P. Pourmand and I. Furó, *J. Phys. Chem. C*, 2017, **121**, 13757–13764.
26 R. Valiullin, *Diffusion NMR of Confined Systems: Fluid Transport in Porous Solids and Heterogeneous Materials*, The Royal Society of Chemistry, Cambridge, 2017.
27 J. D. Jeon and S. Y. Kwak, *Macromolecules*, 2006, **39**, 8027–8034.
28 W. Gorecki, M. Jeannin, E. Belorizky, C. Roux and M. Armand, *J. Phys.: Condens. Matter*, 1995, **7**, 6823.
29 K. Hayamizu, E. Akiba, T. Bando and Y. Aihara, *J. Chem. Phys.*, 2002, **117**, 5929–5939.
30 K. Timachova, H. Watanabe and N. P. Balsara, *Macromolecules*, 2015, **48**, 7882–7888.
31 B. Sun, J. Mindemark, E. V. Morozov, L. T. Costa, M. Bergman, P. Johansson, Y. Fang, I. Furó and D. Brandell, *Phys. Chem. Chem. Phys.*, 2016, **18**, 9504–9513.
32 F. Malz and H. Jancke, *J. Pharm. Biomed. Anal.*, 2005, **38**, 813–823.
33 K. S. W. Sing, in *Studies in Surface Science and Catalysis*, ed. F. Rodriguez-Reinoso, J. Rouquerol, K. S. W. Sing and K. K. Unger, Elsevier, 1991, vol. 62, pp. 1–9.
34 E. O. Stejskal and J. E. Tanner, *J. Chem. Phys.*, 1965, **42**, 288.
35 L. M. Schneider, N. Ihrner, D. Zenkert and M. Johansson, *ACS Appl. Energy Mater.*, 2019, **2**, 4362–4369.
36 H. Fałtynowicz, M. Kułażynski and S. H. Goodman, in *Handbook of Thermoset Plastics*, Elsevier, Amsterdam, 2022, pp. 175–229.
37 A. Gugliuzza, in *Encyclopedia of Membranes*, ed. E. Drioli and L. Giorno, Springer Berlin Heidelberg, 2016, pp. 1801–1802.
38 A. Sienkiewicz, P. Krasucka, B. Charmas, W. Stefaniak and J. Goworek, *J. Therm. Anal. Calorim.*, 2017, **130**, 85–93.
39 C.-Y. Tsai, K.-J. Peng, C.-F. Wang and Y.-L. Liu, *ACS Sustainable Chem. Eng.*, 2020, **8**, 2138–2146.
40 D. C. Martínez Casillas, M. P. Longinotti, M. M. Bruno, F. Vaca Chávez, R. H. Acosta and H. R. Corti, *J. Phys. Chem. C*, 2018, **122**, 3638–3647.
41 Y. Xu, L. Gao, X. Wu, S. Zhang, X. Wang, C. Gu, X. Xia, X. Kong and J. Tu, *ACS Appl. Mater. Interfaces*, 2021, **13**, 23743–23750.
42 W. Liu, S. W. Lee, D. Lin, F. Shi, S. Wang, A. D. Sendek and Y. Cui, *Nat. Energy*, 2017, **2**, 17035.
43 J. Wan, J. Xie, X. Kong, Z. Liu, K. Liu, F. Shi, A. Pei, H. Chen, W. Chen, J. Chen, X. Zhang, L. Zong, J. Wang, L.-Q. Chen, J. Qin and Y. Cui, *Nat. Nanotechnol.*, 2019, **14**, 705–711.
44 L. D. Gelb and K. E. Gubbins, *Langmuir*, 1998, **14**, 2097–2111.
45 M. Laradji, S. Toxvaerd and O. G. Mouritsen, *Phys. Rev. Lett.*, 1996, **77**, 2253–2256.
46 W.-J. Ma, A. Maritan, J. R. Banavar and J. Koplik, *Phys. Rev. A*, 1992, **45**, R5347–R5350.